


Optical spin angular momentum sensitivity of topological nanoflakes

D. Dams ^{*}*Institute of Theoretical Solid State Physics, Karlsruhe Institute of Technology, Kaiserstr. 12, 76131 Karlsruhe, Germany*C. Rockstuhl *Institute of Theoretical Solid State Physics, Karlsruhe Institute of Technology, Kaiserstr. 12, 76131 Karlsruhe, Germany
and Institute of Nanotechnology, Karlsruhe Institute of Technology, Kaiserstr. 12, 76131 Karlsruhe, Germany*

(Received 14 March 2025; revised 29 May 2025; accepted 16 June 2025; published 27 June 2025)

Two-dimensional Chern insulators, characterized by broken time-reversal symmetry and chiral edge states, are a promising platform to engineer exotic light-matter interactions. While most previous studies focused on bulk optical properties in extended media, investigations uncovering the unique photonic features of finite topological structures have been rare. In this work, we consider the optical response in nanoflakes of the prototypical Haldane model, which describes graphene-like systems where time reversal and sublattice symmetry breaking drive a topological phase. A simple argument elucidating the interplay between these fundamental properties and the optical spin angular momentum (SAM) of external light singles out these nanoflakes as prime candidates for SAM-sensitive optics. Building on these insights, we conduct a linear response analysis which reveals highly selective optical behavior, manifesting in strongly enhanced preferential absorption. Our results bridge topological materials and photonics, highlighting a direct link between topological properties and characteristics of electromagnetic radiation.

DOI: [10.1103/sbly-4chz](https://doi.org/10.1103/sbly-4chz)

I. INTRODUCTION

The enhancement and control of light-matter interactions depending on internal characteristics of the electromagnetic radiation involved is a cornerstone of technological progress, with recent advances being made in the fields of energy harvesting [1] and pharmaceutical applications [2] as well as the transfer of angular momentum between light and matter [3].

Of particular importance has been the search for systems capable of highly selective electromagnetic interactions based on specific characteristics of the light, e.g., such as its helicity [4] or optical angular momentum [5]. In recent years, there has been a significant focus on discovering more exotic platforms that enhance and tune these interactions, driven by advancements in the fields of artificial photonic materials [6], hybrid quantum optical and condensed systems [7,8], or tapping into the potential of topological phases of matter [9]. A class of such more exotic material platforms to elevate these preferential interactions could be topological condensed matter systems, which have unveiled intriguing potential in engineering novel light-matter interactions due to their unusual scattering behavior [10]. Despite this potential, the limited research on these materials, particularly finite structures, in

a photonic context hampers conceptual understanding, which could otherwise lead to technological advancements in the future.

To aid in resolving this issue, we further explore the avenue of topological condensed matter systems in a photonic context by investigating nanoflakes described by the prototypical Haldane model of a 2D Chern insulator on a hexagonal lattice. The Haldane model is an attractive platform for many applications and continues to be the subject of recent investigations from a variety of different fields [11–14]. Potential and actual experimental realizations of the Haldane model are numerous, ranging from ultracold fermions [15] to ferromagnetic [16], Moiré [17] or localized Spin systems [18]. Its intrinsically broken time-reversal symmetry (TRS) and the resulting chiral edge currents make this “modified graphene analogon” a natural candidate for a material of strong electromagnetic sensitivity [19]. The magnitude of TRS breaking is parametrically captured in a single variable, corresponding to an internal pseudo-magnetic field strength. Above a certain threshold, this parameter affects a transition from a trivial to a topological phase characterized by the appearance of a chiral conduction channel [20,21].

In the context of nanoflakes, we reveal differential coupling to the spin angular momentum (SAM) of a normally incident plane wave, making them a prime platform for selective light-matter interactions capable of optical filtering and phase manipulation. Understanding the interplay of topological and TRS breaking effects on the electromagnetically selective response of this system, as well as characterizing the strength and robustness of this response, are the prime subjects of our investigation.

^{*}Contact author: david.dams@kit.edu

The rest of this paper is organized as follows: In Sec. II we introduce the concept of SAM in the context of the microscopic Haldane model and discuss its role in the light-matter interactions of topological nanoflakes. We investigate the energetic characteristics of chiral edge states that are essential for understanding the SAM selectivity in Sec. III. Section IV then explores the dipolar response spectra of these nanostructures, revealing strong SAM-selective resonances that emerge as a consequence of chiral edge states. We further investigate the dependence of these resonances on the topological control parameter and discuss their connection to the bulk phase transition. Section V quantifies the degree of optical selectivity by defining a measure for SAM-selective absorption and analyzing its behavior across different parameter regimes. In Sec. VI we study finite-size scaling effects, demonstrating how the response of larger nanoflakes exhibits a redshift and enhanced resonances due to an increasing density of states near the Fermi level. Finally, in Sec. VII we summarize our findings and discuss potential implications for future research and technological applications.

II. OPTICAL SELECTIVITY IN TOPOLOGICAL NANOFLAKES

The remarkable electromagnetic sensitivity of the Haldane model [22] and a closely related relative [23] as homogeneous, infinitely extended media has been previously investigated through a k -space analysis of transition dipole moments, showcasing the emergence of perfect circular dichroism and the resulting implications for valley polarization. The subject of this study, in contrast, is the potential of Haldane nanostructures to host strongly SAM-selective electromagnetic interactions. To this end, we briefly review both the microscopic Haldane model and the concept of optical spin angular momentum, concluding with a physical argument for the Haldane model as a prime candidate to exhibit strongly SAM-dependent optical responses.

We consider nanoflakes of a two-dimensional Chern insulator on a honeycomb lattice in the xy plane under open boundary conditions. The microscopic Hamiltonian is given by [24]

$$H = \delta \sum_i \chi_i a_i^\dagger a_i + t \sum_{\langle i,j \rangle} a_i^\dagger a_j + \lambda \sum_{\langle\langle i,j \rangle\rangle} e^{i v_{ij} \phi} a_i^\dagger a_j, \quad (1)$$

where a_i annihilates an electron at lattice site i and χ_i represents a sublattice indicator function, which we choose as $\chi_i = 1(-1)$ for the A(B) sublattice. The first term involving δ represents a staggered on-site energy that breaks the sublattice symmetry (SLS), leading to a mass gap between the two sublattices. We remove the associated parametric freedom by fixing $\delta = 0.5t$. The second term represents the nearest-neighbor hopping between sublattices with hopping amplitude t set to $t = 1$ eV throughout. The third term describes next-nearest neighbor hopping with amplitude λ and a phase factor parameterized by ϕ . The directionality of these hoppings is enforced by v_{ij} , which is 1 for clockwise and -1 for counterclockwise hoppings. The role played by the next-nearest-neighbor hopping is that of an intrinsic magnetic field, breaking time-reversal symmetry, and is crucial for the topological properties of the model. In the bulk case, it leads

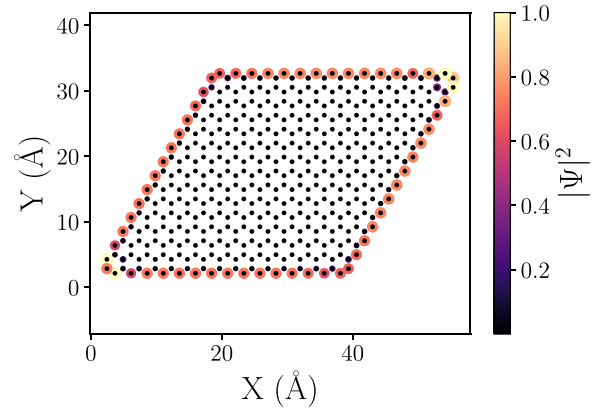


FIG. 1. Exemplary nanoflake described by the Haldane model with $\lambda = 0.3t$. This parameter choice leads to a topological edge state, whose site-resolved absolute value $|\Psi|^2$ is plotted on top of the atomic cores (indicated by black dots).

to a valley-dependent mass term which differs between the K and K' points in the Brillouin zone.

For $\lambda = 0$, the model describes a topologically trivial material with a hexagonal unit cell and broken SLS, akin to MoS_2 [25] or certain varieties of functionalized graphene [26]. For $\lambda \neq 0$, a topological phase transition takes place above a critical threshold given by $\lambda > \frac{\delta}{3\sqrt{3}\sin\phi}$. To focus on the essential topological effects, we specialize it to $\phi = \frac{\pi}{2}$ in concrete simulations, resulting in a single phase transition point at $\lambda > \frac{\delta}{3\sqrt{3}}$. At this value, the bulk system transitions from a trivial to a topological insulating phase characterized by a Chern number of 1, implying the opening of a chiral conduction channel. This channel corresponds to an electronic state strongly localized at the edge of a finite sample, giving rise to a quantized Hall conductivity even in the absence of an external magnetic field, a phenomenon referred to as the anomalous quantum Hall effect. One promising feature about these states lies in their topological protection, making them robust against disorder. The phase diagram of the full Haldane model is displayed in Fig. 2.

In finite samples, the type of edge termination—whether zigzag or armchair—significantly influences the emergence of edge states and their topological protection [27]. Variations in coherence lengths depending on termination make armchair edge states more susceptible to geometric details such as the flake diameter [28]. In contrast, zigzag-edged flakes host states that reliably appear in conjunction with the bulk topological transition. Thus, we consider zigzag-edged nanoflakes to focus on the essential physics at play. An exemplary rhomboid nanoflake in the topological regime, along with an emerging edge state, is displayed in Fig. 1. We have chosen the spatial characteristics of the nanoflakes to agree with typical values for graphene due to its relevance as a potential platform for realizing the Haldane model, e.g., via substrate-induced spin-orbit coupling [29], leading to a distance between atomic nearest neighbors of 1.42 Å. For the main part of this investigation, a prototypical rhombic geometry is chosen due to its inversion symmetry, which controls for effects dependent on spatial symmetry-breaking details and

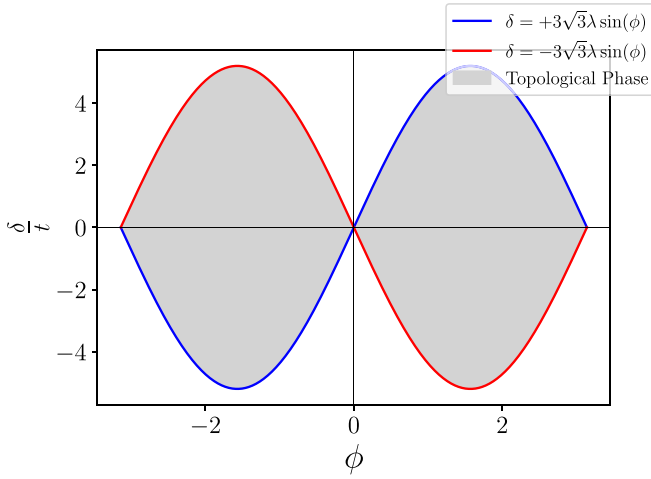


FIG. 2. Phase diagram of the Haldane model showing the topological mass term $\delta = \pm 3\sqrt{3}\lambda \sin(\phi)$ as a function of the complex hopping phase ϕ . The gray region indicates the topologically nontrivial phase (Chern number $C = \pm 1$), where time-reversal symmetry is broken and chiral edge states emerge at finite terminations of the lattice.

in analogy with commonly fabricated graphene nanoribbons [30,31].

Crucially, from the perspective of identifying and investigating electromagnetically selective coupling channels, edge states propagate unidirectionally, i.e., they follow a fixed path around finite samples, either clockwise or counterclockwise. In our convention, a clockwise edge current flow corresponds to $\lambda > 0$. This inherent directionality makes topological nanoflakes of the kind described by Eq. (1) natural candidates for differential coupling to the two SAM components of light, which, in an electromagnetic plane wave as we consider here, manifest as opposing in-plane rotatory directions [32]. To illustrate this potential for selectivity, we focus on the spin angular momentum components E_+ , E_- of a normally incident plane wave. They are given by the projections [32]

$$E_\sigma = \langle \mathbf{e}_\sigma, \mathbf{E} \rangle, \quad (2)$$

where $\sigma = \pm 1$. The (plane wave) circularly polarized basis vectors are defined as

$$\mathbf{e}_\sigma = \frac{1}{\sqrt{2}}(\mathbf{e}_x + i\sigma\mathbf{e}_y). \quad (3)$$

We remark that the above definition of SAM and, further, the separation of total angular momentum into a spin and orbital part are strictly valid only in the normally incident plane wave or paraxial regime, in which case spin and total angular momentum coincide [33]. The associated vector potential of the incident illumination couples to the (paramagnetic) current operator \mathbf{J} of the nanoflake, which is determined by [34]

$$\mathbf{J} = \frac{i}{\hbar}[\mathbf{P}, H]. \quad (4)$$

Here the dipole operator

$$\mathbf{P} = e\mathbf{x} \quad (5)$$

is defined in terms of the elementary charge e and the canonical position operator \mathbf{x} , which we assume to be diagonal in a maximally localized basis [35]. Thus, the analytical expressions for the underlying tight-binding basis functions do not enter the calculation explicitly, as all necessary information is contained in the parametric Hamiltonian given by Eq. (1) and the atomic positions. The projection in Eq. (2) naturally leads to the definition of the positive and negative SAM-sensitive components of the current operator

$$J_\sigma = \langle \mathbf{e}_\sigma | \mathbf{J} \rangle. \quad (6)$$

These SAM-sensitive components are related via Hermitian conjugation,

$$J_+ = J_-^\dagger. \quad (7)$$

The impact of the broken TRS is best illustrated by an argument based on transition rates, in the conceptual spirit of the calculation performed in [22] for the bulk case. To this end, we consider the modulus $|J_{\sigma, nm}|$ of the SAM-sensitive parts of the current operator. In Fig. 3 we display $|J_{\sigma, nm}|$ for rhomboid nanoflakes for different values of λ . The TRS-preserving case of $\lambda = 0$ implies a symmetric rate distribution $|J_{\sigma, nm}| = |J_{\sigma, mn}|$. Increasing λ explicitly breaks TRS and leads to an asymmetric transition rate distribution. Drawing on Fermi's golden rule and Eq. (7), the consequence of SAM-selective coupling becomes apparent: SAM-induced transitions between energy eigenstates favored via J_+ are depressed via J_- and vice versa. In the following, we will explore this consequence in depth by analyzing the dipolar response.

III. EDGE STATE CHARACTERISTICS

In this section, we clarify the role of topological edge states in the SAM-selective response of topological nanoflakes. Based on the physics of infinite and semi-infinite systems, we identify the key characteristics contributing to the SAM selectivity in finite samples and provide numerical evidence to support this claim.

By combining the insights gained from the analysis of infinite [11] and semi-infinite [36] structures described by the Haldane model, some essential characteristics of edge states in topological nanoflakes can be qualitatively discussed. In infinite structures, as shown in [11], incident Gaussian light undergoes a separation into two beams of opposite SAM-polarization. This phenomenon is known as the photonic spin Hall effect and demonstrated to depend intricately on the valley degree of freedom, with optical transitions linked to the band gap. Breaking translational invariance in one direction results in ribbon-like geometries as in [36]. Chiral states manifest, which propagate unidirectionally along the edges of the ribbon. In undoped zigzag geometries, the energy dispersion of the edge states connects the two different valleys, crossing the Fermi level [27].

The finite extent of the nanoflakes considered in the present study completely removes translational invariance. This breaks up the energetic continuum into discrete states, as shown in Fig. 4, requiring the use of a language typically associated with molecular systems. In the trivial phase, we expect the HOMO-LUMO transition energy to approximately match the bulk band gap. However, in the topological phase,

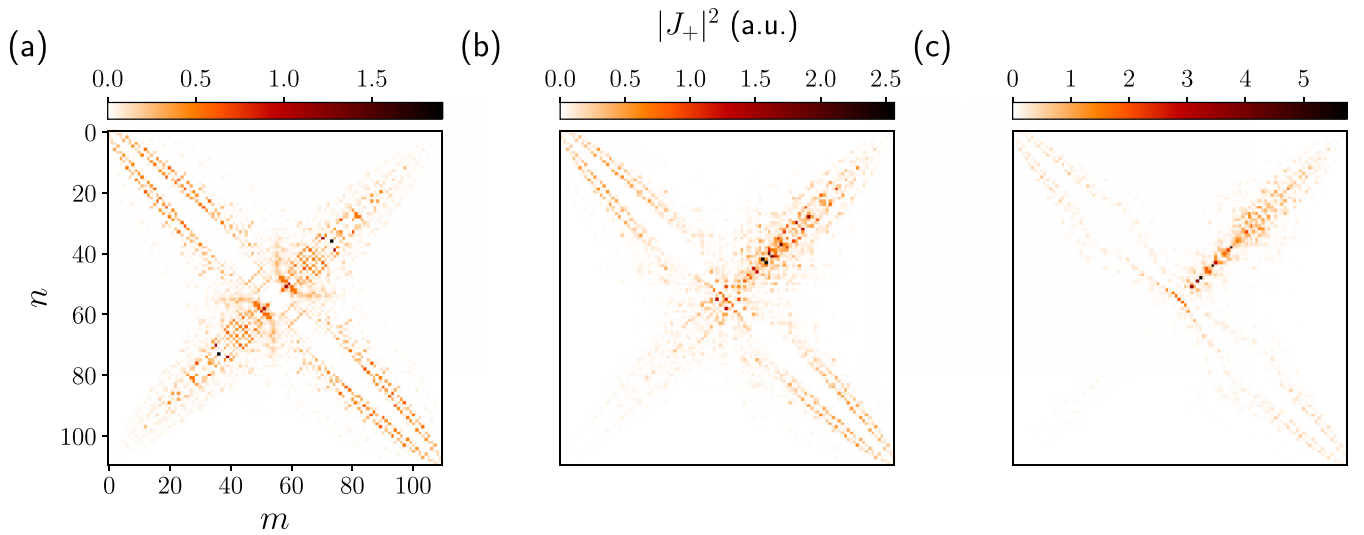


FIG. 3. (a)–(c) Transition matrix elements (modulus squared) of J_+ between different energy eigenstates, labeled by n and m . The underlying system is a rhomboid flake as depicted in Fig. 1 containing 110 atoms for varying values of λ . (a) For $\lambda = 0$, the system is topologically trivial, characterized by the absence of edge states, while TRS is left intact, resulting in a symmetric distribution of transition matrix elements, where $|J_{+,nm}| = |J_{+,mn}|$. (b) An increase in λ to $0.1t$ retains topological triviality. However, with TRS broken, the transition matrix element distribution becomes asymmetric. Since $J_+ = J_-^\dagger$, transitions favored by J_+ are depressed by J_- and vice versa, allowing for differential SAM coupling. (c) Transition matrix elements increase considerably in the topological regime for $\lambda = 0.2t$.

we expect a family of highly localized states to appear in the band gap of the infinite system, roughly corresponding to a “spectral subsample” of the metallic 1D topological bands observed in semi-infinite flakes [36]. The energy spectrum of an exemplary system hosting such localized states is displayed in Fig. 4(b).

Transitions between edge states necessarily occur at energies below the bulk band gap, which implies a low-frequency response dominated by topological effects. The SAM splitting uncovered in [11] for an infinite bulk suggests that these transitions will be distinguished by their sensitivity to different

SAM components of the external illumination. Since we consider a normally incident plane wave, these SAM components correspond to left- and right-handed circular polarizations [37]. It is exactly this low-energy nature of the manifold of edge state transitions that hinders a direct comparison to optical transitions observed in the bulk case, which take place primarily via interband transitions [11].

Finally, we connect these insights to the discussion of the SAM-sensitive matrix elements of the current operator displayed in Fig. 3: The SAM sensitivity and selection rules of an edge state transition can be determined by its associated

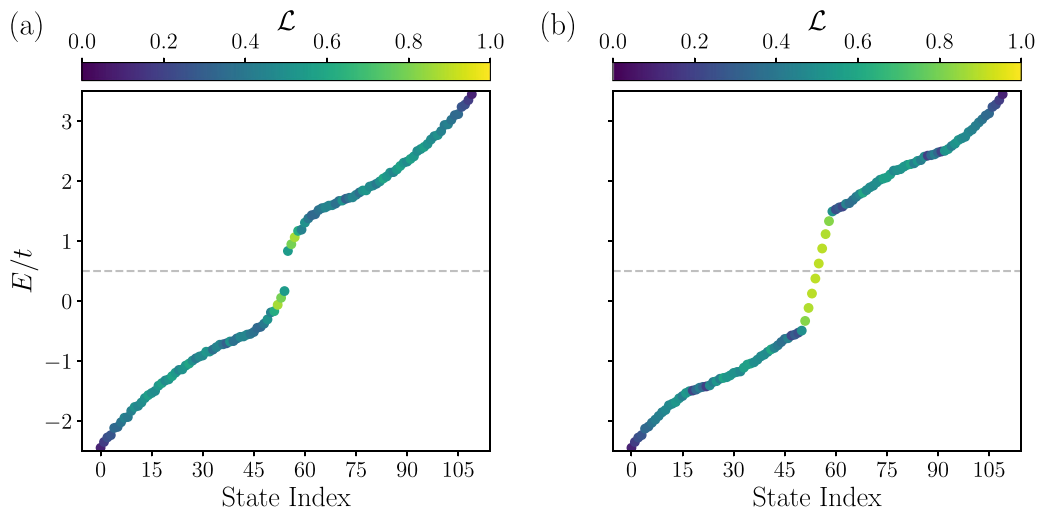


FIG. 4. (a) Energy spectrum of a topologically trivial nanoflake at $\lambda = 0.05t$. The structure is rhomboidal with a width and height of 53 \AA and 30.5 \AA , respectively. It contains 478 atoms in total. The color coding corresponds to the localization metric introduced in Eq. (8). The absence of states around the Fermi level prevents transitions to occur at lower frequencies. (b) Same as in (a), but for the topologically nontrivial case $\lambda = 0.3t$. Strongly localized states around the Fermi level allow low-frequency transitions, making the optical response predominantly topological.

current operator matrix elements. For example, a positive SAM preference of a transition between two edge states labeled by n and m implies $|J_{nm}^+| > |J_{nm}^-|$.

We numerically validate the physical intuition developed above by conducting a spectral analysis of the Hamiltonian describing a finite, N -atomic nanoflake in different topological regimes. To help delineate edge from bulk states, we employ a localization metric. For each eigenstate of the Hamiltonian, we compute the projections onto atomic sites ϕ_i , $i \leq N$. The edge localization \mathcal{L} of an eigenstate is then given by

$$\mathcal{L} = \frac{\sum_{j \text{ edge index}} |\phi_j|^2}{\sum_i |\phi_i|^2}. \quad (8)$$

In Fig. 4 we display the energy spectrum of a rhomboid nanoflake containing 478 atoms in the trivial as well as the topological regime. The trivial regime is indeed characterized by a clearly identifiable HOMO-LUMO gap of $\sim 0.7t$, which roughly corresponds to the expected bulk gap of $\sim 0.5t$. We have checked numerically the convergence of the HOMO-LUMO gap to the bulk band gap for larger systems. At the same time, the topological phase affects the appearance of strongly localized states energetically located in the bulk gap, allowing for optical transitions of much lower frequency. Consequently, the HOMO-LUMO gap of the topological system is considerably reduced, and optical transitions in finite systems take place at frequencies below the bulk band gap. Combined with the properties of the TRS-broken current operator discussed in the previous sections, the low-frequency part of the optical response of topological nanoflakes will be dominated by SAM-selective resonances. We demonstrate this explicitly in the following section employing a linear response analysis.

IV. DIPOLAR RESPONSE SPECTRA

In this section, we study the implications of SAM selectivity in topological nanoflakes of the Haldane model by conducting a linear response analysis of the induced dipole moment. This analysis uncovers SAM-selective resonances, which are stabilized and strengthened by transitions involving edge currents in a parametric regime for λ that closely corresponds to the bulk topological state.

The nanoflakes under consideration are of typical molecular extent, while the wavelength of the incident light exceeds this scale. Consequently, the electromagnetic response of the nanoflakes, dependent on the external field $\mathbf{E}(\omega)$ at frequency ω , is well described by an induced electric dipole moment $\mathbf{p}(\omega)$ according to [38]

$$\mathbf{p}(\omega) = G_{PP}(\omega)\mathbf{E}(\omega). \quad (9)$$

Here G_{PP} is the dipole-dipole correlator, which can be readily computed in the usual Lehmann representation as a 3×3 matrix with components [39]

$$G_{PP,ij}(\omega) = \sum_{nm} P_{nm}^i P_{mn}^j \frac{f_n - f_m}{E_n - E_m + \omega + i\gamma}, \quad (10)$$

where i, j denote Cartesian directions. P_{nm}^i represents the matrix element of the dipole operator between the energy eigenstates labeled by n and m with corresponding energies E_n

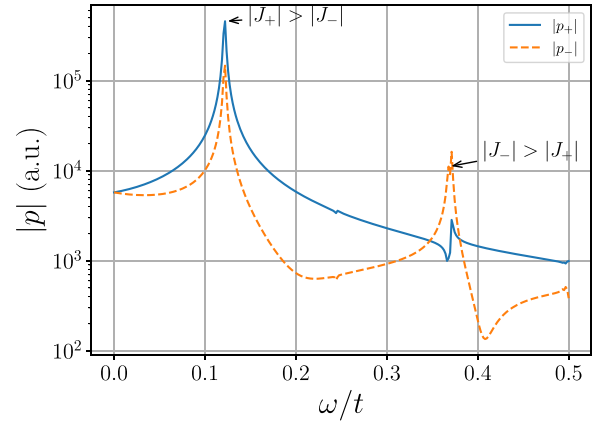


FIG. 5. Dipolar response of a rhomboid nanoflake with a width and height of 53 Å and 30.5 Å, respectively. The flake is characterized by $\lambda = 0.4t$ and considered under unpolarized illumination. The induced dipole moment is decomposed into its SAM-positive and SAM-negative components, revealing a strong differential interaction. Notably, the dominant SAM component changes sign: it is positive at the lower frequency resonance, corresponding to the HOMO-LUMO transition, and becomes negative at higher frequencies. The higher-frequency resonance corresponds to the higher-energy transition closest to HOMO-LUMO.

and E_m and Fermi-Dirac occupations f_n and f_m , specialized to zero temperature. Finally, γ is a numerical broadening parameter, set to 0.001 eV similar to [40]. We remark the following analysis can be carried out equivalently in terms of the current-current correlator, as detailed in Appendix A, which we use as additional validation and to ensure gauge invariance of our results via the Thomas-Reiche-Kuhn (TRK) sum rule [41].

Akin to Eq. (2), we decompose the dipolar response of Eq. (9) to an unpolarized external field into SAM-positive (p_+) and -negative (p_-) components to gain insight into the polarizing behavior of topological nanoflakes. We consider the nanoflake deep in the topological regime by choosing $\lambda = 0.4t$. Figure 5 illustrates the low-frequency ($0 < \omega/t < 0.5$) behavior of the induced dipole moment. A distinct asymmetry emerges in the SAM decomposition: at lower frequencies, the induced dipole moment predominantly aligns with the SAM-positive component, while at the higher end of the considered frequency domain, a resonance associated with a dominant SAM-negative component emerges. Drawing on the discussion in Secs. II and III, this observation can be traced back to the dominance of one microscopic current component over the other at a particular frequency. The low-frequency, SAM-positive resonance corresponds to the HOMO-LUMO transition, where the transition connected to J_+ dominates the one affected by J_- . The SAM-negative resonance arises from the next energetically closest transition above the HOMO-LUMO transition, where the roles of the current operators are reversed—the transition influenced by J_- dominates over that associated with J_+ .

The emergence of optically selective dynamics in the topological phase can thus be understood as a competition between clockwise and counterclockwise microscopic currents. The “fundamental” HOMO-LUMO response is most pronounced

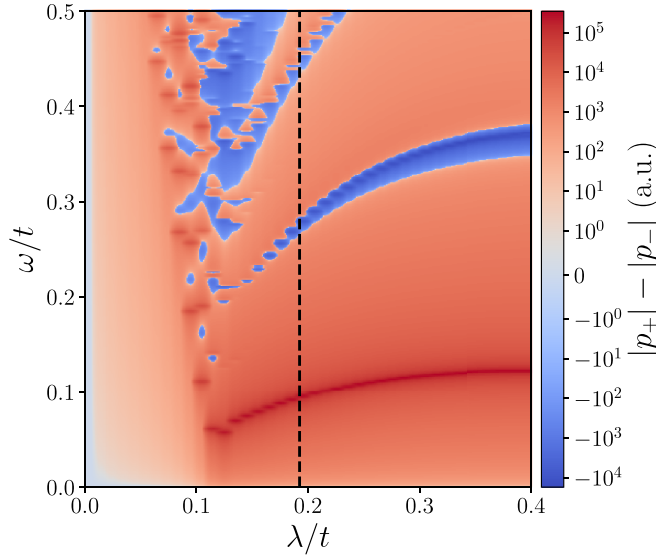


FIG. 6. Differential SAM selection, $|p_+| - |p_-|$, for different values of λ and an identical geometry as considered in Fig. 5. The bulk phase transition is annotated with a dashed black line. For low values of λ , the selectivity is generally weak and shifted towards higher frequencies. The selectivity is highly increased for larger values of λ around the value of the bulk phase transition. Two main resonances manifest, where positive and negative SAM components dominate, respectively. Note that a symmetric log scale is applied, where values in the range of -1 to 1 are mapped linearly, while values beyond this range are scaled logarithmically.

and emerges at the lowest resonant frequency in form of an excess SAM-positive component. While the nonresonant background generally favors the SAM-positive components, the dominant current contribution to the higher-frequency resonance switches sign resulting from the change in the preferred microscopic current interaction channel. The fact that every resonance receives contributions from currents of both directionalities can be traced back to the spatial symmetries of the nanoflake: breaking rhomboid inversion symmetry lifts this spectral degeneracy, as detailed in Appendix B.

Further insight into the onset of electromagnetic selectivity can be provided by studying the dispersion of the selection difference $|p_+| - |p_-|$ as a function of the topological control parameter λ , displayed in Fig. 6. For small values of the topological control parameter λ , the electromagnetic selectivity remains relatively weak and occurs predominantly at higher frequencies. As λ increases and approaches the critical value associated with the bulk phase transition, the selectivity starts to exhibit significant enhancement. A random perturbation analysis, presented in Appendix D and based on a local potential, demonstrates that SAM selectivity in the trivial regime is primarily a system-specific effect arising from the interplay between geometry and inherently broken TRS. In contrast, the selective resonances in the topological regime remain mostly robust against disorder. In this regime, two distinct resonance peaks emerge, each corresponding to a dominant contribution from either the positive or negative SAM component. As discussed above, these resonances correspond to the HOMO-LUMO and the closest transition of higher energy, such that

Fig. 6 implicitly depicts the evolution of these transitions. Their variation with respect to the topological control parameter is considerably smoother, exhibiting a more stable and well-defined functional behavior, with the strength of optical selectivity increasing with λ . It is thus natural to associate these spectral features with the influence of chiral edge states arising in the finite sample.

It is important to note that the preceding discussion is formulated within an independent-particle framework. Previous studies investigating plasmonic collective effects in the semi-infinite Haldane model have demonstrated this approximation to largely suffice in qualitatively explaining dispersive features [42]. Our own RPA-based analysis, detailed in Appendix C, suggests the main impact of electronic correlations in the direct channel to result in a blue shift of the observed resonances. Consequently, our independent-particle picture analysis provides a sufficiently accurate description for the purposes of this analysis.

V. ASSESSING OPTICAL SELECTIVITY

In analogy to commonly employed measures for assessing differential bulk responses to polarized light [43], we define the SAM selectivity s as

$$s = \frac{I_+ - I_-}{I_+ + I_-}, \quad (11)$$

where I_σ represents the absorbed intensity of incident light with the corresponding SAM polarization computed from Eq. (10). This quantity serves as a direct indicator of the differential interaction of the nanoflake with different SAM polarizations.

The computed results are illustrated in Fig. 7, revealing a characteristic variation of SAM selectivity across different parameter regimes. In the region below the approximate threshold associated with the bulk phase transition, comparable to the parameter range examined in Fig. 6, selectivity is still present but manifests in a more irregular and distorted manner. This distortion agrees with the lower intensity response observed in Fig. 6, suggesting a weaker and less well-defined interaction of the system with the incident polarized light.

In contrast, the observed selectivity patterns become more stable and structured as the system enters the regime beyond the bulk phase transition. The resonances become increasingly well defined, aligning with the enhanced response observed in cases of unpolarized incidence. This behavior indicates a pronounced increase in the efficiency of SAM-dependent absorption mechanisms, highlighting the role of the phase transition in modifying the optical and electromagnetic properties of the system.

VI. FINITE-SIZE DIPOLAR SCALING

Up to now, we have considered a prototypical nanoflake of approximately 500 atoms. To ensure the qualitative robustness of our main observation of a strong electromagnetic SAM sensitivity and to study the impact of finite-size effects, we perform a sweep through structures of different sizes ranging from a few hundred atoms to ~ 3200 atoms and study the

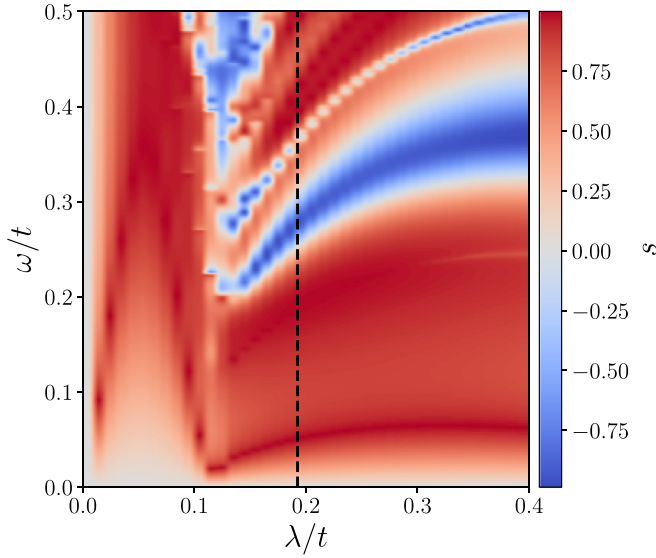


FIG. 7. SAM selectivity s , as defined in Eq. (11). Distinct behavior across different parameter regimes can be observed. Below the region approximately corresponding to the bulk phase transition, similar to the regime shown in Fig. 6, a selectivity is present. Still, it appears to have distorted patterns, consistent with the lower intensity response observed in that figure. In contrast, the patterns become more stable beyond this regime, and resonances are more clearly defined, aligning with the increased yield seen in other figures. The geometry remains unchanged, and the dashed line marks the bulk phase transition.

SAM-selective response. The results from that analysis are displayed in Fig. 8.

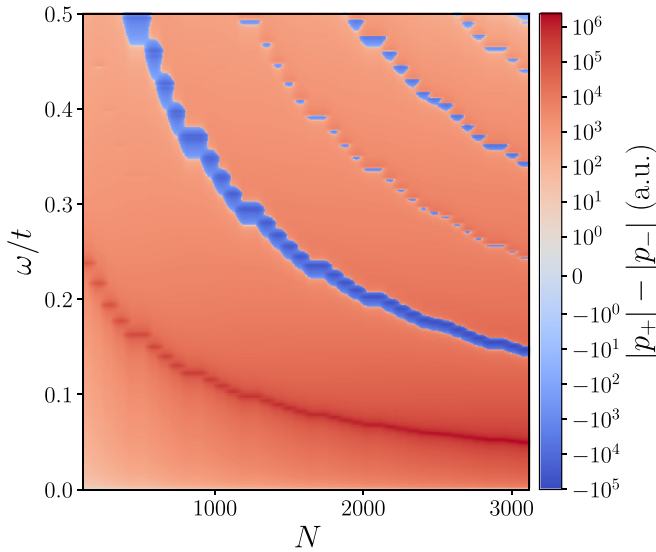


FIG. 8. Differential response $|p_+| - |p_-|$ in Haldane nanoflakes of varying sizes. The control parameter is fixed deep in the topological regime at $\lambda = 0.5t$. The primary effect observed is a redshift and an enhancement of resonances, which is explained in the main text as a consequence of an increased density of states near the Fermi level. A symmetric log scale has been applied as in Fig. 6.

The results reveal a clear trend: as the system size increases, the differential response $|p_+| - |p_-|$ exhibits a pronounced redshift and an overall enhancement of resonance amplitudes. This behavior can be understood as a direct consequence of the increasing density of states (DOS) around the Fermi level. In larger flakes, the discrete energy levels become more closely spaced, leading to a more continuous DOS near relevant optical transition energies. As a result, the system exhibits stronger absorption and enhanced selectivity at slightly lower frequencies. This effect is characteristic of finite-size scaling in topological nanostructures and reinforces the robustness of SAM selectivity in extended systems.

VII. CONCLUSION

In this study, we have explored the optical properties of topological nanoflakes described by the Haldane model and demonstrated their potential for selective light-matter interactions. By systematically analyzing their dipolar response, we have revealed the emergence of strong SAM selectivity, which is directly tied to the presence of chiral edge states. Our findings indicate that this selectivity is highly dependent on the topological control parameter, with a significant enhancement coinciding with the bulk topological phase, where edge states become prominent.

Through a detailed examination of the system's optical response, we have identified key mechanisms driving SAM-selective absorption. Transitions involving topological edge currents exhibit strong polarization-dependent behavior. The interplay of time-reversal symmetry breaking and spatial confinement leads to distinct resonance features, which are robust against moderate variations in system parameters. Thus, these nanoflakes are a promising platform for optically tunable and selective interactions.

Furthermore, we have analyzed finite-size effects and demonstrated that increasing system dimensions leads to a redshift and enhancement of resonances, consistent with the increased density of states near the Fermi level. This behavior suggests that similar optical selection effects could persist in larger-scale realizations, bridging the gap between molecular-scale and mesoscopic devices.

While the present study is primarily concerned with the prototypical Haldane model, it is worthwhile to discuss the effects occurring in its experimentally realizable analogs and elaborate on their potential implications for topological nanoflakes of molecular extent. Buckled Xene monolayers are two-dimensional materials composed of group IV elements. These include silicon (silicene), germanium (germanene), tin (stanene), and lead (plumbene), which are structural analogs of graphene. However, unlike the flat structure of graphene, Xene monolayers exhibit a buckled, out-of-plane configuration [11]. This structural difference gives rise to a pronounced spin-orbit coupling (SOC) in these materials. As a platform for realizing the Haldane model, they are of particular interest, since the staggered onsite potential δ is tunable by applying an external electric field [11]. In combination with its spin-polarized valleys, we expect the optical signatures of topological edge states in nanoflakes to be highly tunable with respect to the externally applied electric field and exhibit an intricate, spin-split resonance structure, similar to the bulk

case reported in [11]. Another possible realization for the Haldane model is constituted by monolayer TMDs, such as MX_2 , where M is molybdenum (Mo) or tungsten (W), and X is sulfur (S) or selenium (Se). In comparison to the aforementioned Xene materials, the in-plane photonic spin Hall shift reported for MoS_2 is considerably larger [11]. This leads us to expect an enhanced resonant behavior at the cost of limited tunability.

In summary, our findings highlight the potential of topological nanostructures as functional elements for optical filtering, polarization control, and light-based information processing. The demonstrated SAM selectivity opens avenues for future experimental realizations in photonic and optoelectronic applications, particularly in materials such as graphene-based systems where Haldane-like physics can be engineered. Future research may extend this work by incorporating dynamical and nonlinear effects, studying different edge terminations, or exploring multiflake interactions to design complex photonic networks with tailored optical responses.

ACKNOWLEDGMENTS

D.D. and C.R. acknowledge support by the German Research Foundation under Grant No. RO 3640/14-1 within Project No. 465163297. We thank Ivan Fernandez-Corbaton for valuable discussions.

DATA AVAILABILITY

The data that support the findings of this article are openly available [49,50].

APPENDIX A: CURRENT-CURRENT CORRELATOR AND TRK SUM RULE

As discussed in Sec. IV, the analysis of the dipolar response can equivalently be formulated in terms of the current-current correlator rather than the dipole-dipole correlator. This equivalence follows from the pointlike nature of the response at molecular scales, which leads to the relation

$$G_{PP} = \frac{1}{\omega^2} G_{JJ}, \quad (\text{A1})$$

where G_{PP} denotes the dipole-dipole correlator and G_{JJ} the current-current correlator.

A fundamental property governing G_{JJ} is the Thomas-Reiche-Kuhn (TRK) sum rule, which ensures gauge invariance and manifests as a vanishing diagonal DC conductivity [41]. This sum rule reflects the fact that the static limit of the current-current response must cancel out, due to the interplay of diamagnetic and paramagnetic current components [44]. To enforce this gauge invariance condition, we impose the TRK sum rule by redefining the current-current correlator as

$$G_{JJ}(\omega) \rightarrow G_{JJ}(\omega) - G_{JJ}(0), \quad (\text{A2})$$

where $G_{JJ}(0)$ represents the static limit of the current-current correlator. This subtraction guarantees that no unphysical static currents are induced and ensures the correct gauge-invariant behavior of the response function.

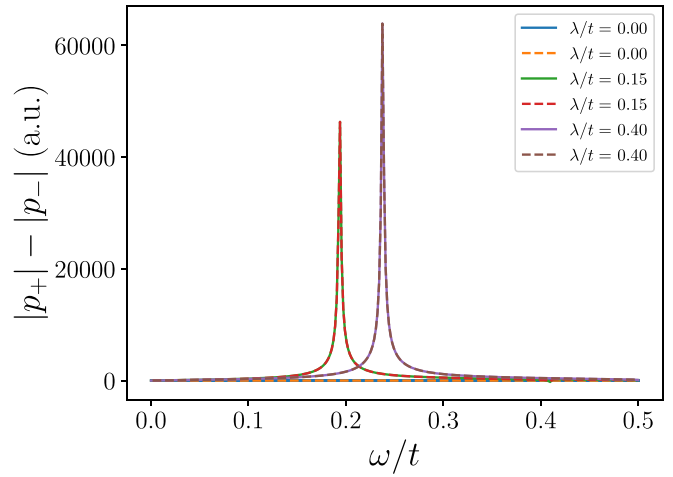


FIG. 9. Comparison of dipolar selection computed from the dipole-dipole (G_{PP} , solid lines) and current-current (G_{JJ} , dashed lines) correlators for rhomboid nanoflakes as displayed in Fig. 1 for different values of the topological control parameter λ . The results show excellent agreement, confirming the consistency of both approaches.

Using Eq. (A1), we compute the dipolar selection $|p_+| - |p_-|$ based on both the dipole-dipole correlator and the current-current correlator. The results, plotted in Fig. 9, demonstrate that the two approaches yield identical outcomes. This agreement validates the computational framework and confirms that the electromagnetic selection properties remain consistent regardless of the formulation chosen.

APPENDIX B: EFFECTS OF SPATIAL SYMMETRY BREAKING

As discussed in detail in Sec. IV and illustrated in Fig. 5, the inversion symmetry of our prototypical rhombic topological nanoflake enforces a spectral degeneracy between SAM-selective resonances. In other words, SAM-positive and SAM-negative resonances predominantly appear in the same spectral regions, leading to a symmetric response.

To break this degeneracy and explore the effects of inversion symmetry breaking, we consider triangular nanoflakes, which lack the spatial inversion symmetry present in the rhombic case. This geometric modification disrupts the symmetry-imposed constraints on the dipolar response, leading to a distinct spectral separation of SAM-positive and SAM-negative resonances. An exemplary spectrum for such a triangular flake, with the same topological control parameter $\lambda = 0.4t$ as in Fig. 5, is presented in Fig. 10. The observed lifting of degeneracy highlights the role of symmetry in shaping the electromagnetic response of topological nanostructures and demonstrates how structural modifications can be used to control SAM-selective interactions.

APPENDIX C: RPA ANALYSIS

The present investigation has thus far been conducted entirely within an effective single-particle framework, neglecting explicit electron-electron correlations. Previous studies have indicated that an independent-particle description

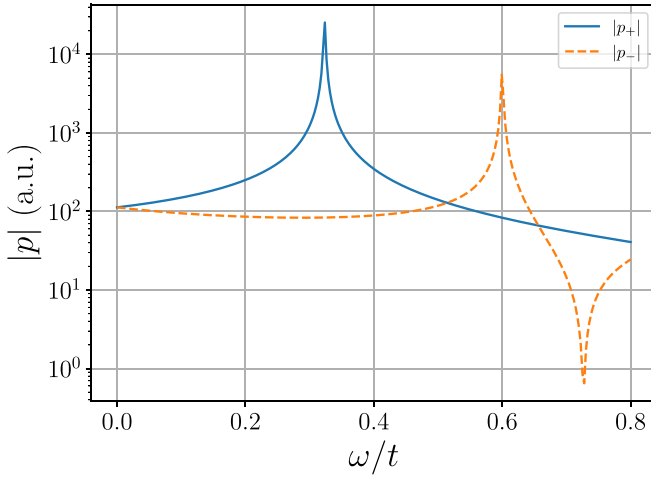


FIG. 10. Dipolar response of an equilateral triangular nanoflake with zigzag edges, characterized by a topological control parameter of $\lambda = 0.4t$, under unpolarized illumination. In contrast to the inversion-symmetric case, the spectral degeneracy of SAM-positive and SAM-negative resonances is lifted, leading to a clear separation of the resonance features.

provides sufficient qualitative insight into the properties of semi-infinite geometries [42]. However, to further establish the robustness of our findings and assess the impact of many-body effects, we extend our analysis by performing a random phase approximation (RPA) study of the system.

A key advantage of optical features that are at least partially rooted in microscopic topology is their inherent robustness against perturbations, including deviations from idealized structures and electron-electron interactions. To validate our results beyond the effective tight-binding picture, we incorporate direct Coulomb interactions by performing an RPA analysis following the approach established in [39]. This is done by isolating the Coulomb matrix C , which captures direct-channel interactions between the p_z -like orbitals within the nanoflake.

To systematically assess the role of electronic interactions, we introduce a dimensionless scaling parameter $c \in [0, 1]$, which controls the interaction strength. We then compute the RPA dipole-dipole correlator as a function of c , from which we extract the magnitude of the electromagnetic dipolar selection $|p_+| - |p_-|$.

The interaction matrix elements U_{ijkl} are defined in terms of their standard real-space representation:

$$U_{ijkl} = \int d\mathbf{r} \int d\mathbf{r}' \bar{\phi}_i(\mathbf{r}) \bar{\phi}_j(\mathbf{r}') \frac{1}{|\mathbf{r} - \mathbf{r}'|} \phi_k(\mathbf{r}') \phi_l(\mathbf{r}), \quad (\text{C1})$$

where $\phi_i(\mathbf{r})$ denotes the basis functions, which we take to be p_z -like atomic orbitals. This choice is motivated by the fact that the Haldane model under consideration reduces to the standard tight-binding description of graphene in the limit $\lambda = \delta = 0$.

The Coulomb matrix C is extracted from the full electron interaction matrix using the conventional definition:

$$C_{ij} = U_{ijji}. \quad (\text{C2})$$

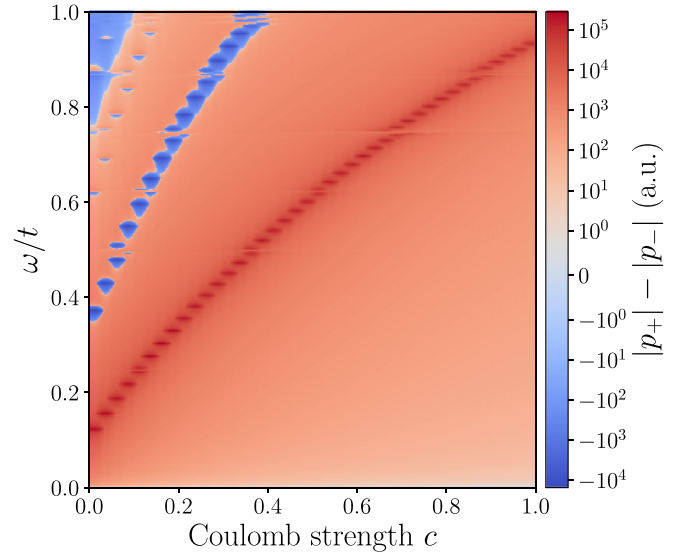


FIG. 11. Impact of electron-electron interactions on the dipolar response of a rhombic nanoflake, analyzed within the RPA framework. The results correspond to the same system as in Fig. 5, with the inclusion of direct-channel Coulomb interactions parameterized by a dimensionless interaction strength c . The main effect observed is a blueshift of the resonance features, while the qualitative structure of the electromagnetic dipolar selection $|p_+| - |p_-|$ remains intact. Such an observation suggests that the key mechanisms underlying SAM selectivity are robust against electronic interactions. A symmetric log scale has been applied as in Fig. 6.

We take analytical values for the Coulomb matrix elements for p_z orbitals in graphenic structures from [45]. To control the interaction strength, we scale the Coulomb matrix by the dimensionless factor $c \in [0, 1]$.

To compute the response function, we define the non-interacting site-resolved density-density correlator as [46]

$$[G_{nn}]_{ab}(\omega) = \sum_{ij} \frac{f_j - f_i}{E_j - E_i + \omega + i\gamma} \psi_{ia}^* \psi_{ib} \psi_{jb}^* \psi_{ja}, \quad (\text{C3})$$

where this quantity is a matrix indexed by the sites of the nanoflake. The RPA-corrected dipole-dipole correlator, $\tilde{G}_{PP}(\omega)$, is obtained by summing all bubble diagrams to include electron-electron interactions and contracting with the Cartesian components i of the site positions $R_{i,a}$. It is given by [39]

$$M = [1 - cG_{nn}(\omega)C]^{-1}G_{nn}(\omega), \quad (\text{C4})$$

$$\tilde{G}_{PP,ij}(\omega) = \sum_{a,b} R_{i,a} M_{ab} R_{j,b}. \quad (\text{C5})$$

The results presented in Fig. 11 correspond to the same rhombic nanoflake as in Fig. 5, now including RPA-corrected interactions. The key observation is that the primary effect of electron-electron interactions is a blueshift of the resonance features. At the same time, the qualitative structure of the electromagnetic dipolar selection $|p_+| - |p_-|$ remains essentially unchanged.

This finding serves as strong evidence for the general robustness of the presented results within a more complete

many-body framework. The fact that the essential features of the SAM-selective response persist suggests that potential experimental realizations do not require an exact microscopic realization of an idealized system. Instead, the topological and geometric properties of the structure play the dominant role in shaping the optical response, making the observed effects resilient to interaction-induced modifications.

APPENDIX D: DISORDERED POTENTIAL ANALYSIS

In this Appendix, we analyze the resilience of the observed optical selectivity in the presence of disorder. To this end, we introduce a random local potential that perturbs the onsite hopping rates in Eq. (1), similar to previous studies on disordered topological systems [47]. The disorder is implemented as follows:

$$t \rightarrow t + r, \quad (\text{D1})$$

where r is a stochastic perturbation sampled from a Gaussian distribution $\mathcal{N}(0, t)$. In Fig. 12 we present numerical results for the same system analyzed in Fig. 6, now incorporating the random disorder modification to the onsite hoppings. In the trivial phase (before reaching the threshold value of λ for the bulk phase transition), the disorder significantly disrupts the optical response, leading to a qualitative breakdown of any discernible resonant patterns. This suggests that in the absence of topologically protected states, the electromagnetic response is highly sensitive to perturbations, likely due to its dependence on geometric and symmetry-based factors that are easily altered by disorder and have been demonstrated lead to pronounced modifications in the plasmonic response of graphene nanostructures [48].

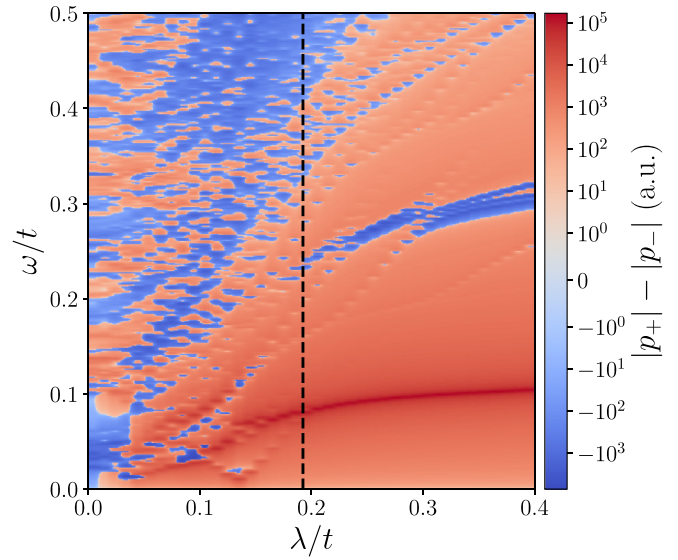


FIG. 12. Impact of disorder on the optical selectivity of the Haldane model. The selective resonances in the topological regime remain intact, highlighting their robustness against perturbations.

Conversely, in the topological phase, the selective resonances persist despite the presence of disorder. In particular, the “fundamental” HOMO-LUMO response discussed in Sec. IV remains clearly identifiable. This stability is a hallmark of topological protection: the chiral edge states affecting SAM selectivity are robust against moderate local perturbations, as they do not rely on fine-tuned material properties but rather on global topological invariants.

-
- [1] Z. Dong, F. Yang, and J. S. Ho, Enhanced electromagnetic energy harvesting with subwavelength chiral structures, *Phys. Rev. Appl.* **8**, 044026 (2017).
 - [2] G. K. E. Scriba, Chiral electromigration techniques in pharmaceutical and biomedical analysis, *Bioanal. Rev.* **3**, 95 (2011).
 - [3] S. Parkin, G. Knüner, T. A. Nieminen, N. R. Heckenberg, and H. Rubinsztein-Dunlop, Measurement of the total optical angular momentum transfer in optical tweezers, *Opt. Express* **14**, 6963 (2006).
 - [4] A. Qu, L. Xu, C. Xu, and H. Kuang, Chiral nanomaterials for biosensing, bioimaging, and disease therapies, *Chem. Commun.* **58**, 12782 (2022).
 - [5] A. Schimmoller, S. Walker, and A. S. Landsman, Photonic angular momentum in intense light-matter interactions, *Photonics* **11**, 871 (2024).
 - [6] A. B. Khanikaev and A. Alú, Topological photonics: Robustness and beyond, *Nat. Commun.* **15**, 931 (2024).
 - [7] J. D. Cox, M. R. Singh, G. Gumbs, M. A. Anton, and F. Carreno, Dipole-dipole interaction between a quantum dot and a graphene nanodisk, *Phys. Rev. B* **86**, 125452 (2012).
 - [8] A. Babaze, E. Ogando, P. E. Stamatopoulou, C. Tserkezis, N. A. Mortensen, J. Aizpurua, A. G. Borisov, and R. Esteban, Quantum surface effects in the electromagnetic coupling between a quantum emitter and a plasmonic nanoantenna: Time-dependent density functional theory vs. semiclassical Feibelman approach, *Opt. Express* **30**, 21159 (2022).
 - [9] O. Dmytruk and M. Schiró, Controlling topological phases of matter with quantum light, *Commun. Phys.* **5**, 271 (2022).
 - [10] L. Ge, T. Zhan, D. Han, X. Liu, and J. Zi, Unusual electromagnetic scattering by cylinders of topological insulator, *Opt. Express* **22**, 30833 (2014).
 - [11] M. Shah, M. S. Anwar, R. Asgari, and G. Xianlong, Photonic spin Hall effect in Haldane model materials, *Phys. Rev. B* **109**, 235418 (2024).
 - [12] S. Mitra, Á. Jiménez-Galán, M. Aulich, M. Neuhaus, R. E. F. Silva, V. Pervak, M. F. Kling, and S. Biswas, Light-wave-controlled Haldane model in monolayer hexagonal boron nitride, *Nature (London)* **628**, 752 (2024).
 - [13] S. Traverso, M. Sassetti, and N. Traverso Ziani, Emerging topological bound states in Haldane model zigzag nanoribbons, *npj Quantum Mater.* **9**, 9 (2024).
 - [14] P. Mai, B. E. Feldman, and P. W. Phillips, Topological Mott insulator at quarter filling in the interacting Haldane model, *Phys. Rev. Res.* **5**, 013162 (2023).
 - [15] G. Jotzu, M. Messer, R. Desbuquois, M. Lebrat, T. Uehlinger, D. Greif, and T. Esslinger, Experimental realization of the topological Haldane model with ultracold fermions, *Nature (London)* **515**, 237 (2014).

- [16] H. S. Kim and H.-Y. Kee, Realizing Haldane model in Fe-based honeycomb ferromagnetic insulators, *npj Quantum Mater.* **2**, 20 (2017).
- [17] W. Zhao, K. Kang, Y. Zhang, P. Knüppel, Z. Tao, L. Li, C. L. Tschirhart, E. Redekop, K. Watanabe, T. Taniguchi *et al.*, Realization of the Haldane Chern insulator in a moiré lattice, *Nat. Phys.* **20**, 275 (2024).
- [18] S. K. Kim, H. Ochoa, R. Zarzuela, and Y. Tserkovnyak, Realization of the Haldane-Kane-Mele model in a system of localized spins, *Phys. Rev. Lett.* **117**, 227201 (2016).
- [19] C. Ding and M. Zhao, Chiral response in two-dimensional bilayers with time-reversal symmetry: A universal criterion, *Phys. Rev. B* **108**, 125415 (2023).
- [20] J. Li, S. Sanz, N. Merino-Díez, M. Vilas-Varela, A. García-Lekue, M. Corso, D. G. de Oteyza, T. Frederiksen, D. Peña, and J. I. Pascual, Topological phase transition in chiral graphene nanoribbons: From edge bands to end states, *Nat. Commun.* **12**, 5538 (2021).
- [21] V. Peano, M. Houde, C. Brendel, F. Marquardt, and A. A. Clerk, Topological phase transitions and chiral inelastic transport induced by the squeezing of light, *Nat. Commun.* **7**, 10779 (2016).
- [22] K. Ghalamkari, Y. Tsumi, and R. Saito, Perfect circular dichroism in the Haldane model, *J. Phys. Soc. Jpn.* **87**, 063708 (2018).
- [23] M. Vila, N. T. Hung, S. Roche, and R. Saito, Tunable circular dichroism and valley polarization in the modified Haldane model, *Phys. Rev. B* **99**, 161404(R) (2019).
- [24] F. D. M. Haldane, Model for a quantum Hall effect without Landau levels: Condensed-matter realization of the “parity anomaly”, *Phys. Rev. Lett.* **61**, 2015 (1988).
- [25] M. Gmitra, D. Kochan, P. Högl, and J. Fabian, Trivial and inverted Dirac band gaps and the emergence of quantum spin Hall states in graphene on transition-metal dichalcogenides, *Phys. Rev. B* **93**, 155104 (2016).
- [26] G. B. Liu, W. Y. Shan, Y. Yao, W. Yao, and D. Xiao, Three-band tight-binding model for monolayers of group-VIB transition metal dichalcogenides, *Phys. Rev. B* **88**, 085433 (2013).
- [27] N. Hao, P. Zhang, Z. Wang, W. Zhang, and Y. Wang, Topological edge states and quantum Hall effect in the Haldane model, *Phys. Rev. B* **78**, 075438 (2008).
- [28] K. Kondo and R. Ito, Quantum spin Hall phase in honeycomb nanoribbons with two different atoms: Edge shape effect to bulk-edge correspondence, *J. Phys. Commun.* **3**, 055007 (2019).
- [29] F. Calleja, H. Ochoa, M. Garnica, S. Barja, J. J. Navarro, A. Black, M. M. Otrokov, E. V. Chulkov, Y. H. W. Son, G. Pratzner *et al.*, Spatial variation of a giant spin-orbit effect induces electron confinement in graphene on Pb islands, *Nat. Phys.* **11**, 43 (2015).
- [30] S. Mishra, X. Yao, Q. Chen, K. Eimre, O. Gröning, R. Ortiz, M. D. Giovannantonio, J. C. Sancho-García, J. Fernández-Rossier, C. A. Pignedoli *et al.*, Large magnetic exchange coupling in rhombus-shaped nanographenes with zigzag periphery, *Nat. Chem.* **13**, 581 (2021).
- [31] S. Lindenthal, D. Fazzi, N. F. Zorn, A. A. E. Yumin, S. Settele, B. Weidinger, E. Blasco, and J. Zaumseil, Understanding the optical properties of doped and undoped 9-armchair graphene nanoribbons in dispersion, *ACS Nano* **17**, 18240 (2023).
- [32] C. Cohen-Tannoudji, J. Dupont-Roc, and G. Grynberg, *Photons and Atoms: Introduction to Quantum Electrodynamics* (Wiley-VCH, Berlin, 1997), Chap. 1.
- [33] I. Fernandez-Corbaton, X. Zambrana-Puyalto, and G. Molina-Terriza, Helicity and angular momentum: A symmetry-based framework for the study of light-matter interactions, *Phys. Rev. A* **86**, 042103 (2012).
- [34] T. G. Pedersen, Graphene fractals: Energy gap and spin polarization, *Phys. Rev. B* **101**, 235427 (2020).
- [35] D. Vanderbilt, *Berry Phases in Electronic Structure Theory: Electric Polarization, Orbital Magnetization and Topological Insulators* (Cambridge University Press, Cambridge, 2018).
- [36] H. Jürß and D. Bauer, Topological edge-state contributions to high-order harmonic generation in finite flakes, *Phys. Rev. B* **106**, 054303 (2022).
- [37] I. Fernandez-Corbaton, M. Fruhnert, and C. Rockstuhl, Objects of maximum electromagnetic chirality, *Phys. Rev. X* **6**, 031013 (2016).
- [38] J. D. Jackson, *Classical Electrodynamics*, 3rd ed. (Wiley, New York, 1999).
- [39] S. Thongrattanasiri, A. Manjavacas, and F. J. García de Abajo, Quantum finite-size effects in graphene plasmons, *ACS Nano* **6**, 1766 (2012).
- [40] M. M. Müller, M. Kosik, M. Pelc, G. W. Bryant, A. Ayuela, C. Rockstuhl, and K. Slowik, Energy-based plasmonicity index to characterize optical resonances in nanostructures, *J. Phys. Chem. C* **124**, 24331 (2020).
- [41] M. Schüller, J. A. Marks, Y. Murakami, C. Jia, and T. P. Devereaux, Gauge invariance of light-matter interactions in first-principle tight-binding models, *Phys. Rev. B* **103**, 155409 (2021).
- [42] H. Schlömer, Z. Jiang, and S. Haas, Plasmons in two-dimensional topological insulators, *Phys. Rev. B* **103**, 115116 (2021).
- [43] T. Stauber, T. Low, and G. Gómez-Santos, Chiral response of twisted bilayer graphene, *Phys. Rev. Lett.* **120**, 046801 (2018).
- [44] G. M. Andolina, F. M. D. Pellegrino, V. Giovannetti, A. H. MacDonald, and M. Polini, Cavity quantum electrodynamics of strongly correlated electron systems: A no-go theorem for photon condensation, *Phys. Rev. B* **100**, 121109(R) (2019).
- [45] P. Potasz, A. D. Güçlü, and P. Hawrylak, Spin and electronic correlations in gated graphene quantum rings, *Phys. Rev. B* **82**, 075425 (2010).
- [46] J. D. Cox and F. Javier García de Abajo, Electrically tunable nonlinear plasmonics in graphene nanoislands, *Nat. Commun.* **5**, 5725 (2014).
- [47] T.-C. Yi, S. Hu, E. V. Castro, and R. Mondaini, Interplay of interactions, disorder, and topology in the Haldane-Hubbard model, *Phys. Rev. B* **104**, 195117 (2021).
- [48] F. Aguilón, D. C. Marinica, and A. G. Borisov, Plasmons in graphene nanostructures with point defects and impurities, *J. Phys. Chem. C* **125**, 21503 (2021).
- [49] D. Dams, M. Kosik, M. Müller, A. Ghosh, A. Babaze, J. Szczuczko, G. W. Bryant, C. Rockstuhl, M. Pelc, and K. Slowik, Granad—Simulating graphene nanoflakes with adatoms (unpublished).
- [50] D. Dams, Haldane model code repository, https://github.com/GRANADlauncher/granad-scripts/tree/main/haldane_array (2025).